Electronic Supplementary information

A highly fluorescent pH sensing membrane for the alkaline pH range incorporating a BODIPY dye

Mandy Hecht, Werner Kraus, Knut Rurack *

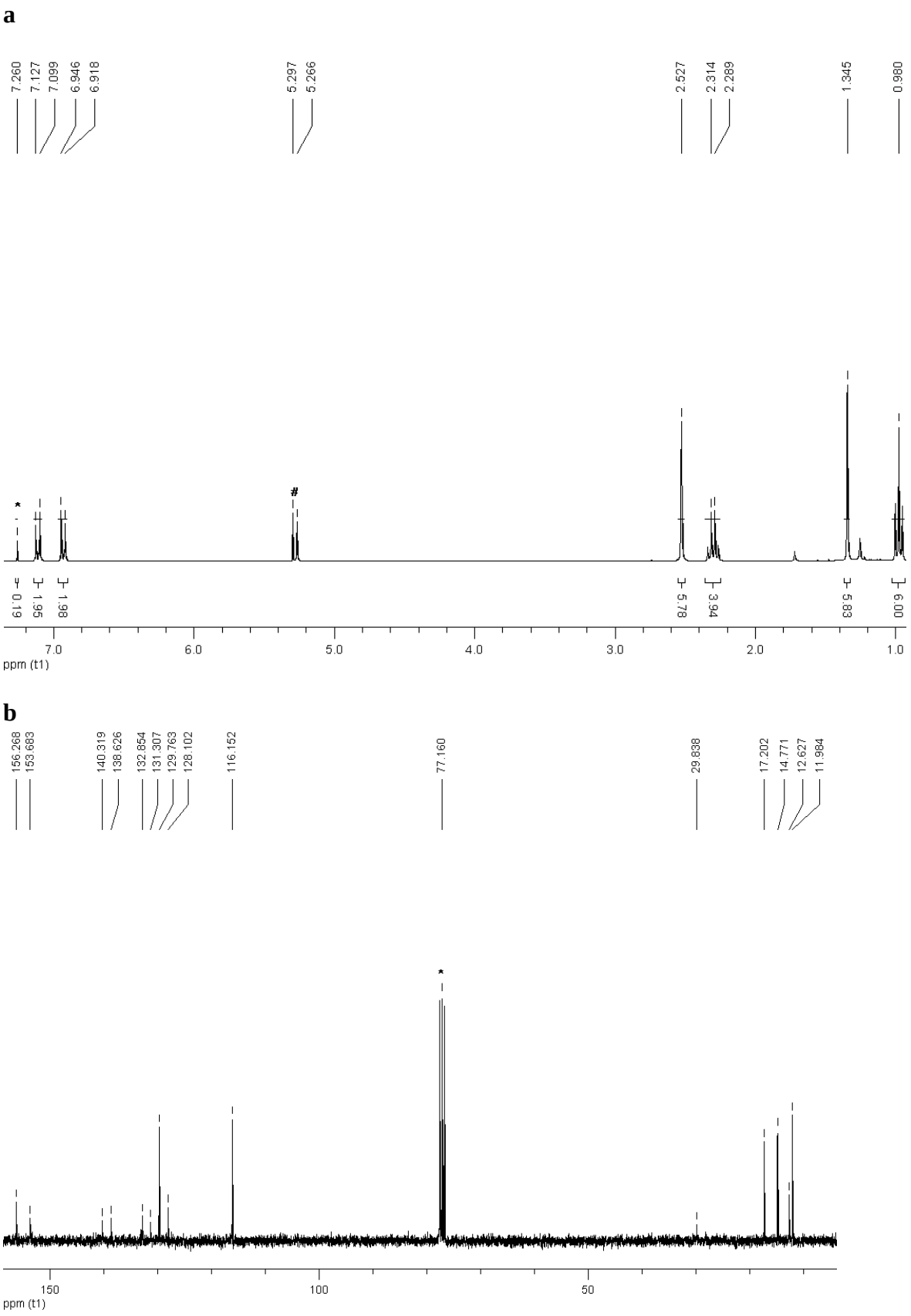

Figure S1. ^{1}H NMR (a) and ^{13}C NMR (b) of **1** in CDCl3. * and # indicate the residual solvent signals and CH_2Cl_2 impurities, respectively.

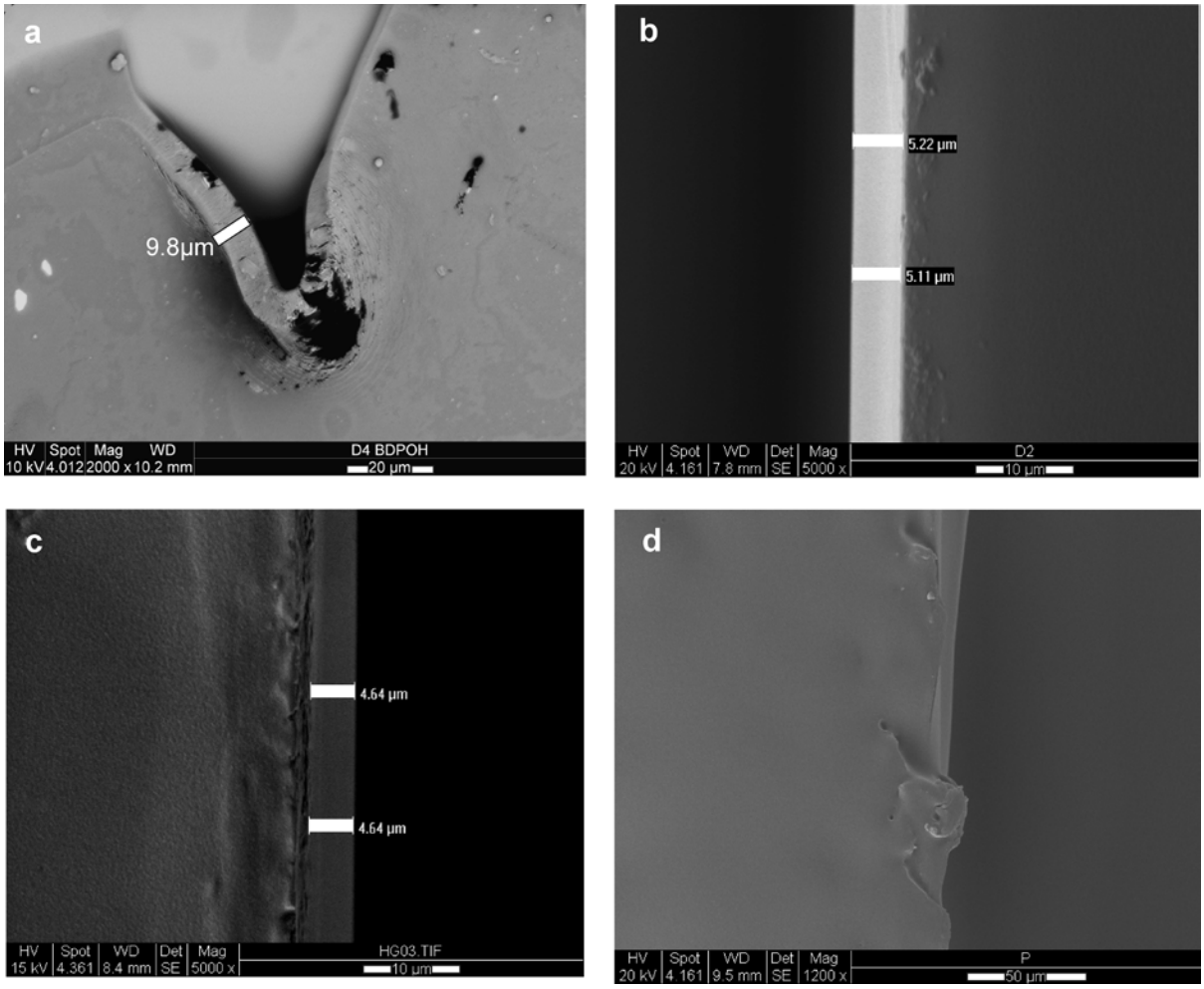

Figure S2. a) Detached polymer on glass support; variation of film thickness on glass support b) D2C1 c) D3D1; d) polymer D4 on polymer support.

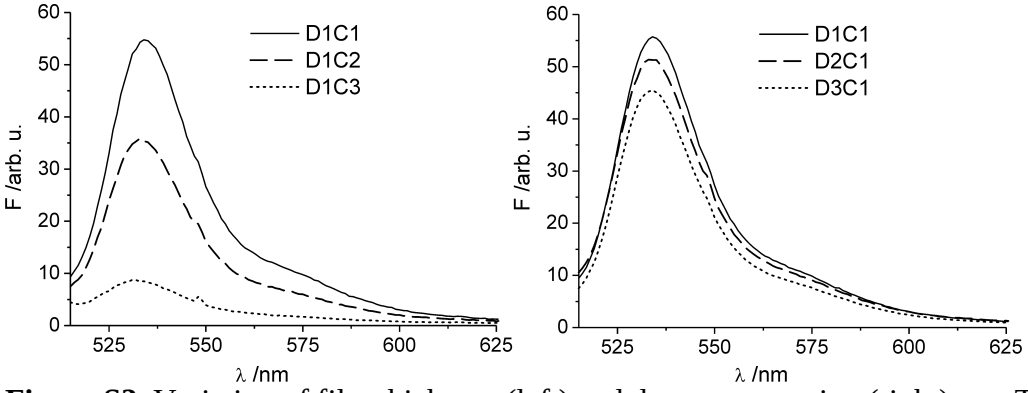

Figure S3. Variation of film thickness (left) and dye concentration (right), see Table 1.

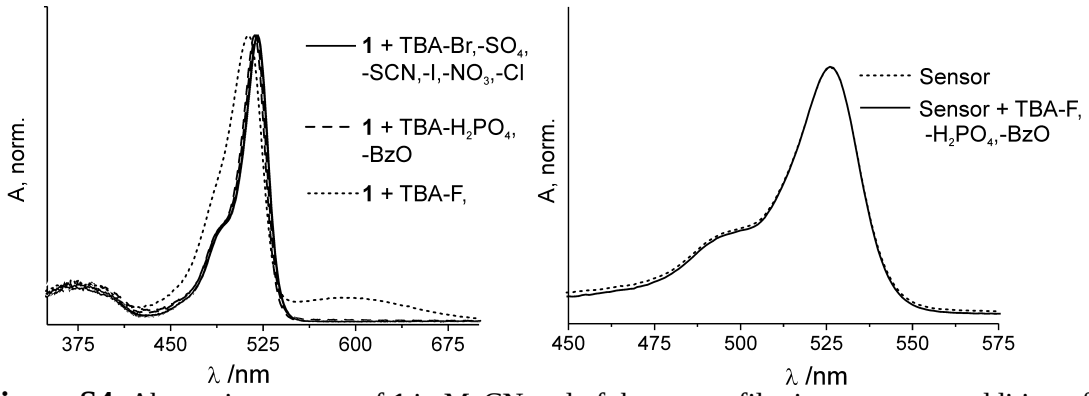

Figure S4. Absorption spectra of **1** in MeCN and of the sensor film in water upon addition of relevant anions (c_{anion} = 7.5 µM).

Figure S5. Visible response of **1** to various anions under UV-light a) in EtOH/H_2O b) in MeCN.

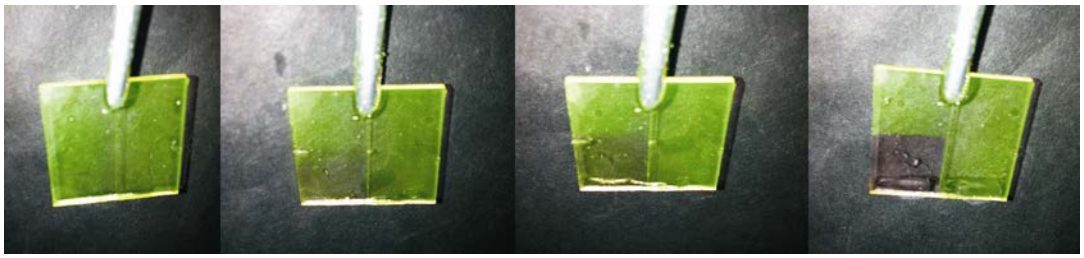

Figure S6. Visible response of the sensor to pH (left to right: pH = 9.0; 10.5; 11.2; 13.0). RGB values were determined using the image editing program GIMP 2.6. and were mathematically transferred to their corresponding CIE values. The average of the colour ratios of sensor **1** and reference **2** were plotted against pH.

Table S1. Formal XPS elemental compositions of used epoxy supports.

Element	*Nexterion E*	*PolyAn 3D Epoxy*
Na	0.46	-
O	62.51	9.57
N	0.30	-
C	9.51	90.25
Si	23.43	0.26
Zn	0.79	-
B	2.96	-
Mg	1.55	-
CO-content	72.02	99.82

Table S2. Average fluorescence readings and corresponding pH values obtained for three different samples; samples were filtrated before measurement to remove suspended solids and fine sediments.

Spiking [a)]	*Sample 1* [b)]		*Sample 2* [c)]		*Sample 3* [d)]	
	F_{532nm} /10^6 *cts*	*pH*	F_{532nm} /10^6 *cts*	*pH*	F_{532nm} /10^6 *cts*	*pH*
no	4.97 ± 0.11	7.44	4.83 ± 0.11	7.93	4.76 ± 0.10	7.51
yes	2.89 ± 0.06	11.34	2.17 ± 0.04	11.56	2.79 ± 0.05	11.40

[a)] All samples (2.5 mL) were spiked with 0.3 mL 0.1 M KOH. [b)] Sample 1: surface water from Landwehrkanal, river kilometre 6.1 (Hallesches Tor), Berlin. [c)] Sample 2: influent water from sewage treatment plant "Teltowkanal Wassmannsdorf", Berlin. [d)] Sample 3: effluent from same sewage treatment plant.

1 X-ray structural analysis

Besides the results given in the main text and listed in Tables S2 and S3, the average B-N bond lengths is around 1.537(3) Å, whereas the B-F bond lengths differ from 1.384(2) Å (B1-F2) and 1.416(3) Å for B1-F1, the latter resulting in an interaction between the OH group and F1 with d_{OH-F} = 1.943 Å and d_{O-F} = 2.795 Å. This intermolecular interaction creates chains of molecules in the diagonal a-c direction (Figure S7). The molecular packing in the crystal structure is given in Figure S8. Due to the centro symmetry and the arrangement of the molecules, the π-π stacking between adjacent pyrromethene rings was not observed in the crystal packing.

The N1-B-N2, F1-B-F2, N1-B-F2, and N2-B-F1 angles are 107.75(15)°, 108.11(16)°, 111.72(17)°, and 109.40(17)°, respectively. These data are in good agreement with the corresponding values of the BF_2N_2 tetrahedron configurations published previously for related analogues[1, 2].

Table S3. Crystal data and structure refinement for **1**.

	1
Empirical formula	$C_{23}H_{27}BF_2N_2O$
Formula weight	396.28
Temperature [K]	296(2)
Wavelength [Å]	0.71073
Crystal system, space group	monoclinic, P2(1)/n (No. 14)
Unit cell dimensions [Å,°]	a = 10.5132(16)
	b = 10.5783(16)
	c = 19.315(16)
	β = 97.647(9)
Volume [$Å^3$]	2128.9(5)
Z / Calculated density [g/cm^3]	4 / 1.236
Absorption coefficient [mm^{-1}]	0.087
F(000)	840
Crystal size [mm]	0.31 x 0.28 x 0.09
θ range for data collection [°]	2.10 to 27.50
Limiting indices	$-13 \le h \le 8$,
	$-13 \le k \le 13$,
	$-24 \le l \le 24$
Reflections collected / unique	16033 / 4826
R(int)	0.1049
Absorption correction	semi-empirical from equivalents
Refinement method	Full-matrix least-squares on F^2
Data / restraints / parameters	4826 / 0 / 266
Goodness-of-fit on F^2	0.855
Final R indices [I>2sigma(I)]	R1 = 0.0531 , wR2 = 0.1310
R indices (all data)	R1 = 0.0996, wR2 = 0.1484
Largest diff. peak and hole [e / $Å^3$]	0.230 and -0.231

Table S4. Selected bond lengths and angles for **1**.

Distance [Å]	BDP-OH	Angle [°]	BDP-OH
N1 - B1	1.538(3)	C11 - N1 – C8	107.77(16)
N2 - B1	1.537(3)	C11 - N1 – B1	126.86(17)
N1 - C11	1.357(2)	C8 - N1 - B1	125.24(16)
N1 - C8	1.402(2)	C13 - N2 – C12	108.20(16)
N2 - C13	1.356(3)	C13 - N2 – B1	126.41(16)
N2 - C12	1.402(2)	C12 - N2 – B1	125.37(15)
F1 - B1	1.416(3)	F2 - B1 - F1	108.11(16)
F2 - B1	1.384(2)	F2 - B1 - N2	111.05(17)
O1 - C1	1.374(2)	F1 - B1 - N2	109.40(17)
		F2 - B1 - N1	111.72(17)
		F1 - B1 - N1	108.77(16)
		N2 - B1 - N1	107.75(15)
		O1 - C1 - C2	123.10(18)
		O1 - C1 - C6	117.58(18)

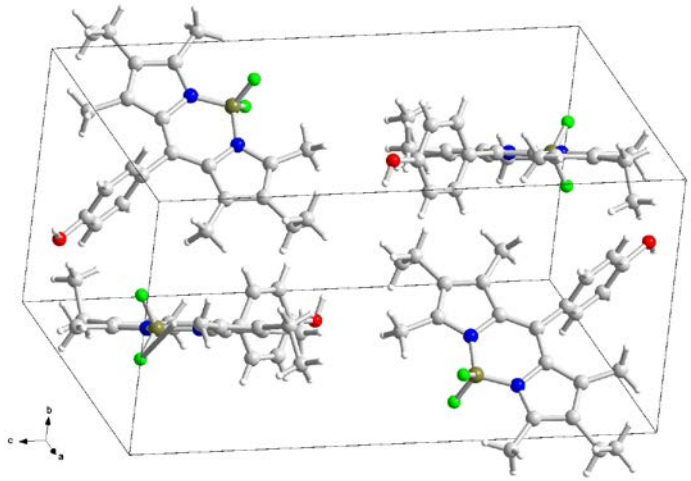

Figure S7. Arrangement of the molecules of **1** in the unit cell. Grey spheres denote carbon atoms, red spheres denote oxygen atoms, green spheres denote fluorine atoms, dark green spheres denote boron atoms and white spheres denote hydrogen atoms.

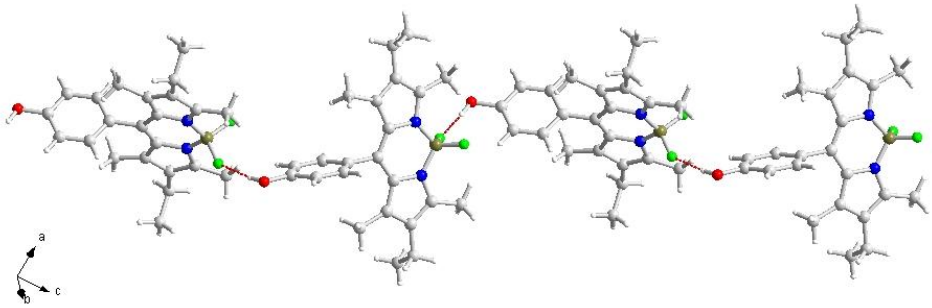

Figure S8: Chain of molecules of **1** with H bonds (d_{OH-F} = 1.943 Å d_{O-F} = 2.795 Å).

2 Quantum chemical calculation results of 1 and its deprotonated form

Quantum chemical calculations were carried out on **1** and its deprotonated form to obtain a better understanding of the nature of the efficient quenching process in the latter. Optimization of the S_0 ground state geometries in the gas phase was performed with the density functional theory (DFT) method employing the hybrid functional B3LYP with a 6-31G basis set and energy-minimized as implemented in Gaussian 03.[3] Figure S9 collects the frontier molecular orbitals of **1**, fully ground-state-optimized **1**$^-$ and the perpendicular form of **1**$^-$, **1**$^-$(perp). For the latter structure, only the dihedral angles holding the central BODIPYs 6-membered ring and the *meso*-phenyl group in orthogonal orientation were fixed at 90° while all other coordinates of the molecule were allowed to optimize. Table S5 contains the calculated properties for the vertical excitation of the energy-minimized ground-state geometries.

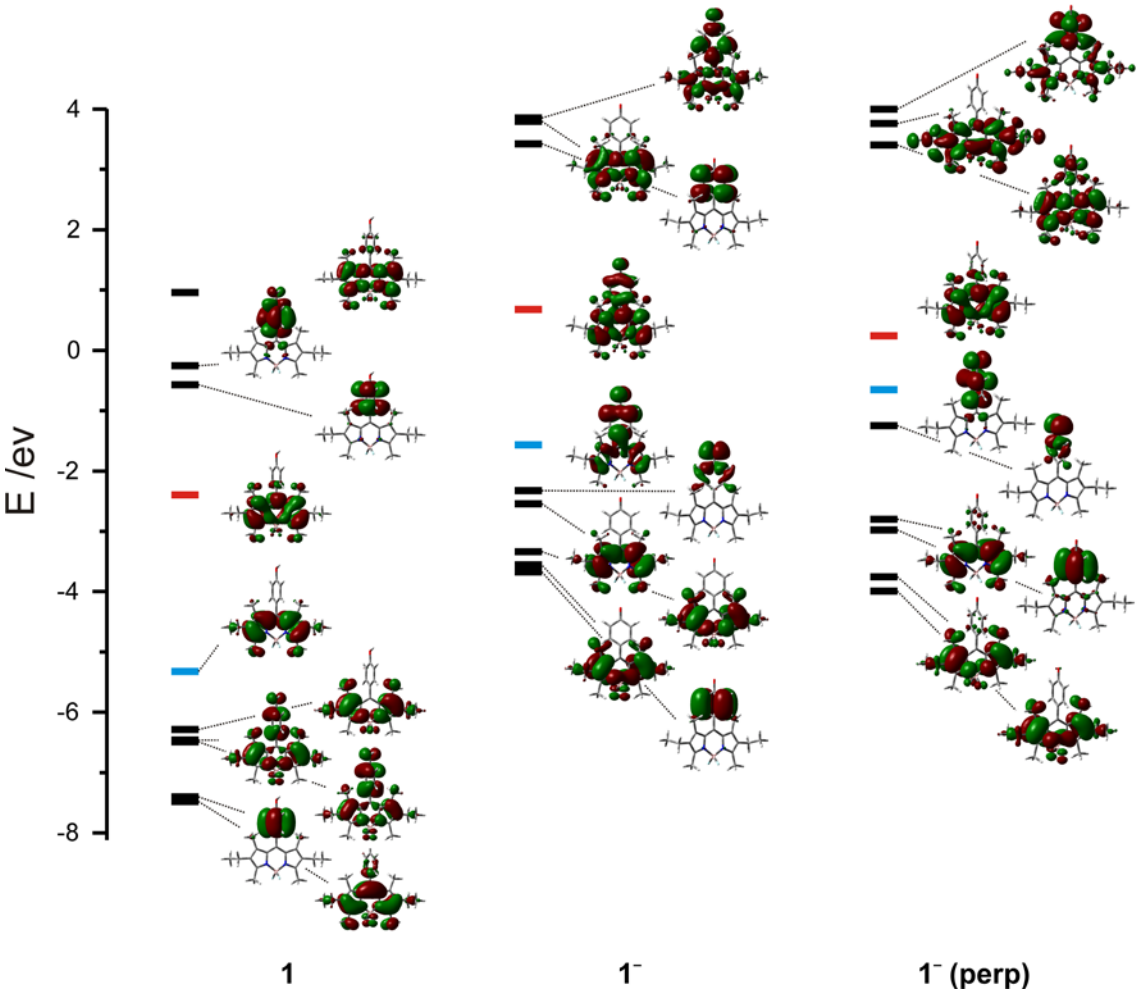

Figure S9. Frontier molecular orbitals of geometry-optimized **1**, **1**$^-$ and **1**$^-$(perp); LUMO in red, HOMO in blue.

Table S5. Calculated properties for the vertical excitation of the energy-minimized ground-state geometries of **1**, **1**$^{-}$ and **1**$^{-}$(perp).

	$\lambda_{S_n \leftarrow S_0}(n)$ /nm [a]	f [b]	$\Delta\mu_{S_n - S_0}$ /D [c]	Orbitals (coefficients) [d]
1	430.0 (1)	0.427	–1.6	HOMO–LUMO (0.54), HOMO–1–LUMO (0.29)
	370.8 (2)	0.250	0.1	HOMO–LUMO (–0.22), HOMO–1–LUMO (0.60)
	366.7 (3)	0.005	19.6	HOMO–2–LUMO (0.47), HOMO–3–LUMO (0.52)
	356.2 (4)	0.038	–0.8	HOMO–2–LUMO (0.49), HOMO–3–LUMO (–0.45)
	298.3 (5)	0.005	9.9	HOMO–LUMO+1 (0.7)
1^{-}	549.5 (1)	0.160	1.7	HOMO–LUMO (0.38), HOMO–1–LUMO (0.52)
	541.3 (2)	0.232	–0.4	HOMO–LUMO (0.38), HOMO–1–LUMO (–0.45)
	413.9 (3)	0.374	6.1	HOMO–2–LUMO (0.61), HOMO–3–LUMO (–0.19)
	360.3 (4)	0.091	4.5	HOMO–2–LUMO (0.15), HOMO–3–LUMO (0.65)
	340.5 (5)	0.004	–2.9	HOMO–5–LUMO (0.69)
1^{-}(perp)	5216.0 (1)	0.000	–3.4	HOMO–LUMO (0.7)
	1205.4 (2)	0.001	4.5	HOMO–1–LUMO (0.7)
	489.0 (3)	0.000	–7.7	HOMO–2–LUMO (0.11), HOMO–3–LUMO (0.69)
	414.6 (4)	0.456	1.9	HOMO–2–LUMO (0.55), HOMO–4–LUMO (0.26)
	358.2 (5)	0.192	–0.2	HOMO–2–LUMO (–0.20), HOMO–4–LUMO (0.62)
	354.8 (6)	0.006	–2.7	HOMO–LUMO+1 (0.69)

[a] Wavelength of the transition. [b] Oscillator strength of the transition. [c] Dipole moment difference between ground (μ_0) and respective excited (μ_n) state. [d] MOs involved in the transitions.

Table S5 shows that for **1** the lowest oscillator-strong transition is found at 430 nm in the gas phase, followed by a weaker transition at 371 nm and several distinctly weaker transitions up to ca. 260 nm (the next oscillator-strong transition involves S_8 and is centered at 258 nm). The

high-energy deviation of the reproduction of the absolute transition energies is known for BODIPY dyes and DFT calculations, see discussion in ref. 4. However, despite this hypsochromic displacement for the gas phase transitions, DFT calculations have been found to reproduce the trends upon chemical modification of the calculated BODIPY structures rather well.[4] Consideration of the delocalization of the molecular orbitals involved in the S_1 and S_2 transitions in Figure S8 reveals that both HOMO–1 and HOMO as well as LUMO are all delocalized virtually exclusively on the BODIPY core. These transitions are thus characteristic for allowed BODIPY-centered transitions and correspond to the highly emissive dye in its protonated form. Singlet-triplet energy gaps are >0.8 eV for the two lowest transitions and the only small gap of 0.04 eV found for the mixed HOMO–2/HOMO–3–LUMO transition (S_3) does not open an efficient quenching channel because this transition is rather high-lying. Considering that the dipole moment change of this transition is rather large (19.6 D), this transition should occur as the S_2 transition in a highly polar environment (ΔE_{MeCN} = 3.22 eV for gas-phase S_3 and 3.34 eV for gas-phase S_2). However, the energy difference to S_1 still amounts to $\Delta E_{S2–S1}$(MeCN) = 0.34 eV in a polar solvent, rendering a quenching influence less likely. The theoretical results thus reproduce well the solution findings.

The situation is different for the fully geometry-optimized **1**$^-$. The calculations predict a reduction of the interannular twisting angle from 87° in **1**, which agrees well with the angle found in the X-ray analysis, to 50.2° in **1**$^-$. Along with this planarization, oscillator-strong transitions at longer wavelength are predicted, namely at 541 and 549 nm. However, the solution spectra of the deprotonated form of **1** do not show any hints of a sizeable absorption band at wavelengths >530 nm in MeCN or EtOH/H_2O. Given the systematic underestimation of the absolute transition energies, such values should correspond to actual bands at >600 nm, which have not been recorded in any of the solution based studies here. Apparently, the planarization obtained theoretically for the gas phase does not occur in water. We thus fixed the dihedral angles along the *meso*-bond in a perpendicular fashion and repeated the optimization process, arriving at **1**$^-$(perp), which is ca. 32 kJ mol^{-1} less stable than **1**$^-$ in the gas phase. Table S5 shows that the results obtained for vertical excitation of **1**$^-$(perp) agree well with the spectroscopic results measured in solution. Two extremely low-energy-based transitions are found which both possess an oscillator strength of virtually zero and are thus strongly forbidden. These transitions involve complete orbital separation as is obvious from Figure S8; HOMO and HOMO–1 are localized entirely on the phenolate fragment whereas

LUMO is delocalized over the BODIPY core. As would be expected for such decoupled structures, singlet-triplet energy differences are very small with ΔE_{S-T} = 0.01 eV for the S_1/T_1 pair and 0.02 eV for the S_2/T_2 pair. Efficient non-radiative deactivation would thus be expected for $\mathbf{1}^-$ (perp). In agreement with the solution data, the first transition of sizeable oscillator strength is found at 414 nm, i.e., slightly hypsochromically shifted compared to that of **1** at 430 nm. Efficient intramolecular electron transfer-type quenching is thus the main deactivation pathway in $\mathbf{1}^-$. Since $\mathbf{1}^-$ is expected to decay non-radiatively and shows blue-shifted absoption spectra, the experimental findings of a slight blue-shift in absorption and virtually no shift in fluorescence are well-supported by theory.

3 References

1. Y.-H. Yu, Z. Shen, H.-Y. Xu, Y.-W. Wang, T. Okujima, N. Ono, Y.-Z. Li and X.-Z. You, *J. Mol. Struct.*, 2007, **827**, 130-136.
2. R. Ziessel, L. Bonardi, P. Retailleau and G. Ulrich, *J. Org. Chem.*, 2006, **71**, 3093-3102.
3. M. J. Frisch e t al. Gaussian 03, revision D.01, Gaussian, Inc., Wallingford CT, 2004.
4. Y.-W. Wang, A. B. Descalzo, Z. Shen, X.-Z. You, K. Rurack, *Chem. Eur. J.*, 2010, **16**, 2887-2903.